Effects of obstacles on inertial focusing and separation in sinusoidal channels: An experimental and numerical study

Haotian Cha [a,1], Hoseyn A. Amiri [b,c,1], Sima Moshafi [d,e,1], Ali Karimi [f], Ali Nikkhah [g], Xiangxun Chen [a], Hang T. Ta [a,h], Nam-Trung Nguyen [a,*], Jun Zhang [a,*]

[a] Queensland Micro- and Nanotechnology Centre, Griffith University, Nathan, Queensland 4111, Australia
[b] Department of Biomechanics, School of Mechanical Engineering, Iran University of Science and Technology, Narmak, Tehran 16846-13114, Iran
[c] George W. Woodruff School of Mechanical Engineering, Parker H. Petit Institute for Bioengineering and Biosciences, Georgia Institute of Technology, Atlanta, GA 30332, USA
[d] Department of Mechanical Engineering, Faculty of Engineering, Kharazmi University, Tehran 15719-14911, Iran
[e] Department of Mathematics and Statistics, Georgia State University, Atlanta, GA 30303, USA
[f] Department of Chemical and Petroleum Engineering, Sharif University of Technology, Tehran 14588-89694, Iran
[g] Department of Mechanical and Aerospace Engineering, University at Buffalo, The State University of New York, Buffalo, NY 14260, USA
[h] Bioscience Discipline, School of Environment and Science, Griffith University, Nathan, Queensland 4111, Australia

A B S T R A C T

Inertial microfluidics manipulates and separates microparticles based on the finite inertia of the fluid at high flow speed. In inertial microfluidics, modifying the geometry by embedding periodic micro-obstacles into curvilinear channels is emerging as a promising strategy to improve inertial focusing and separation. This work systematically investigated the influence of micro-obstacles on inertial focusing and developed a high-resolution microfluidic device for particle and cell separation. First, we developed numerical modelling to simulate the migration trajectories of particles. Then, we studied the effects of various obstacles on the inertial focusing in the sinusoidal channels. The concave obstacles were more effective in tuning particle inertial focusing and separation than convex obstacles. Furthermore, the square concave obstacle channel could offer the highest separation resolution. Finally, we developed a microfluidic device based on square concave obstacle channel, and applied it for the high-efficiency separation of polystyrene beads and U87MG cancer cells from the blood.

1. Introduction

Microfluidics is the science and technology of systems that process or manipulate fluids within microchannels of tens to hundreds of micrometres (Whitesides, 2006). Microfluidics offers exceptional benefits of small sample volumes, low cost, high resolution, small footprints and rapid processing (Thompson et al., 2014; Pappas and Wang, 2007). Microfluidic manipulation techniques can be categorized as passive and active approaches based on the source of manipulating forces. In active methods, external acoustic (Collins et al., 2014; Lin et al., 2012), electrical (Dalili et al., 2021; Pethig, 2010), and magnetic (Pamme, 2006; Nam-Trung, 2012) force fields are utilized to manipulate particles. In contrast, passive techniques exploit the intrinsic hydrodynamic effects such as viscoelastic forces (D'Avino et al., 2017; Lu et al., 2017), inertial forces (Di Carlo, 2009; Zhang, 2016), hydrophoresis (Yan, 2018; Choi and Park, 2007), and deterministic lateral displacement (Hochstetter, 2020; Huang et al., 2004). Active methods generally have a better

accuracy, however, the throughput is typically limited. In contrast, passive techniques are straightforward, easy to use and capable of higher throughput.

Inertial microfluidics is one of the passive microfluidic techniques for microparticle manipulation and separation based on the finite inertia of the fluid at a relatively high speed (Tang et al., 2020; Bazaz et al., 2020; Amini et al., 2014). Inertial microfluidics possesses superior features of high throughput, simplicity, precise manipulation and low cost. It has been extensively applied for the separation of circulating tumour cells (Ren, 2021), fractionation of blood cells (Wu et al., 2012), purification of single stem cells (Nathamgari, 2015), isolation of extracellular vesicles (Tay, 2021) and filtration of bacteria (Warkiani et al., 2015) etc. Inertial microfluidics works based on two inertial effects due to the finite inertia of the fluid at high speed: (i) inertial migration and (ii) secondary flow. Inertial migration refers to migration of randomly dispersed particles toward specific radial equilibria when passing through a tube under a laminar Poiseuille flow (Segre, 1961). Two inertial lift forces are

---

* Corresponding authors.
  E-mail addresses: nam-trung.nguyen@griffith.edu.au (N.-T. Nguyen), jun.zhang@griffith.edu.au (J. Zhang).
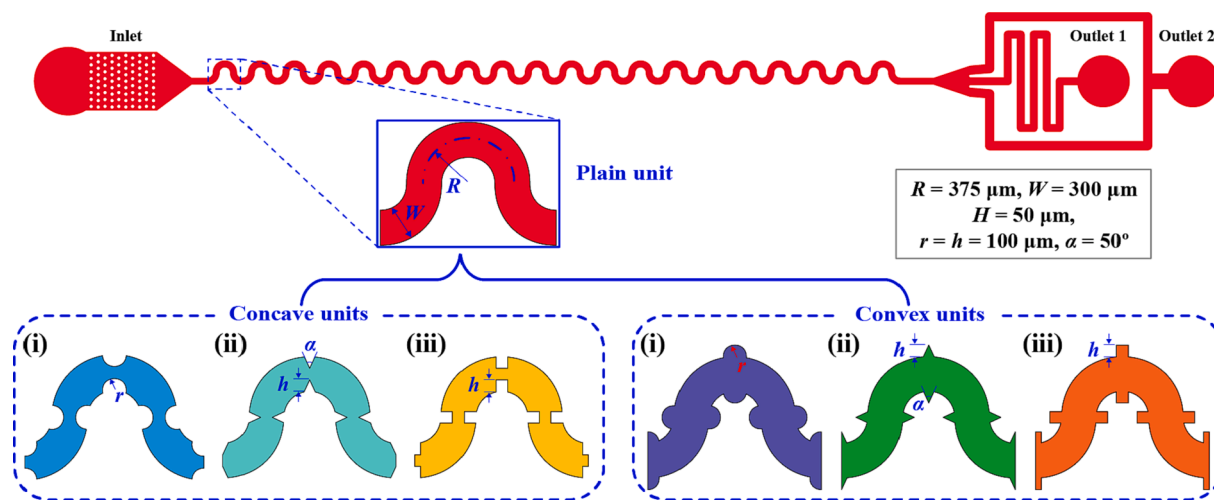[1] Equally contributed.

Fig. 1. Schematics of the plain sinusoidal microchannel, concave obstacle, and convex obstacle channels with shapes of (i) circular, (ii) triangular, and (iii) square.

recognized as the cause: the shear gradient lift force - the interaction of the curvature of the fluid velocity profile with a particle, and the wall lift force - the flow field interaction between the suspending particle and the adjacent walls (Martel and Toner, 2014). In addition to the inertial lift forces, curved channels induce secondary flows because of fluid momentum mismatch between the centre and near-wall regions. The counterbalance of secondary drag and inertial lift forces modifies the equilibrium positions of particles within the channel cross-section (Martel and Toner, 2013). As a result, the final location of particles is highly affected by the channel geometry, flow characteristics, and particle size (Zhou and Papautsky, 2021; Zhou and Papautsky, 2013; Kim et al., 2016).

To date, many geometries have been studied for particle inertial focusing and separation including straight (Bhagat et al., 2008; Zhou et al., 2013), contraction and expansion (Lee et al., 2013; Li, 2016), spiral (Wu et al., 2012; Kuntaegowdanahalli et al., 2009), helix (Paiè et al., 2017; Asghari et al., 2019), 3D composition (Chen, 2019), square wave and sinusoidal microchannels (Zhang et al., 2014; Ying and Lin, 2019; Rodriguez-Mateos et al., 2021; Zhang, 2019). Recently, embedding periodic micro-obstacles in channels is emerging as a novel method to further improve and optimize inertial focusing and separation (Shen, 2017; Shi et al., 2021; Zhao et al., 2022; Lu et al., 2020; Cha, 2022). However, the current understanding of the influence of micro-obstacles on inertial focusing is still limited and even contradictory among the limited reports. For example, Ai's group observed that adding micro contractions in a curvilinear channel could improve the separation resolution (Lu et al., 2020). In contrast, our recent work showed that micro-obstacles embedded in the sinusoidal channels could tune the flow rates for particle separation, but no significant improvement in separation resolution was found (Cha, 2022). This indicates that a more comprehensive study is in demand.

In this work, we systematically investigated the influence of micro-obstacles on inertial focusing in the sinusoidal microchannel numerically and experimentally. We developed a numerical modelling method to predict the migration trajectories of particles. Various obstacle shapes - circular, triangular and square with different sizes were added or subtracted from the sinusoidal channels as convex and concave obstacle channels. We found that concave obstacles were more effective in tuning the flow rate for particle inertial focusing and separation. In addition, the square obstacles could improve particle separation resolution. Finally, we developed a high-resolution microfluidic device, and characterized the separation performance of the device using polystyrene microbeads and blood samples spiked with cancer cells.

2. Materials and methods

2.1. Design and fabrication

In this work, the whole channel comprised of 20 repetitive sinusoidal periods integrated with different concave and convex microstructures, Fig. 1. The height (H), width (W), and curvature radius (R) of the primary sinusoidal channels were 50 μm, 300 μm, and 375 μm, respectively. We defined the sinusoidal channel without obstacles and with inward and outward obstacles as plain, concave-obstacle and convex-obstacle channels, respectively. Obstacles of circular, triangular, and square types were patterned symmetrically on both sidewalls of the channels. To make dimensions consistent between various obstacles, the heights ($h = r$) of obstacles were kept constant at 100 μm. All the microfluidic devices in this work were fabricated by standard photolithography and polydimethylsiloxane (PDMS) soft lithography (Whitesides et al., 2001).

2.2. Particle preparation

Two sets of spherical polystyrene microbeads of 10-μm and 15-μm diameter were suspended in deionized (DI) water. The particle-weight ratio in the suspension was approximately 0.05%. Tween 20 (Sigma-Aldrich, product no. P9416) was dissolved in the suspension as a surfactant at a weight ratio of 0.1% to prevent particle aggregation. To investigate the particle separation cut-off size, we used poly(methyl methacrylate) (PMMA) beads with a continuous size from 5 μm to 20 μm (Cospheric LLC, Santa Barbara, CA, USA). We dispersed 65 mg particle powder into 25 mL DI water and stirred well to obtain a uniform suspension. To characterize the binary separation performance of the devices, a binary mixture of 10- and 15-μm polystyrene particles was prepared in DI water, and their concentrations were 2.25×10^6 counts/mL and 6.46×10^3 counts/mL, respectively.

2.3. Blood and cancer cells preparation

Blood was sourced from the Australian Red Cross Blood Service. Griffith University Human Research Ethics Committee approved the use of human blood samples with protocol number 2021/598. All experiments were performed in compliance with the relevant laws and institutional guidelines. U87MG Human Glioblastoma cells were purchased from American Type Tissue Culture Collection (ATCC, Manassas, VA, USA). The cell culture reagents were purchased from Thermo Fisher Scientific (Waltham, MA, USA). Cells were cultured in T75 flasks in Dulbecco's Modified Eagle Medium (DMEM) with low glucose, 10%
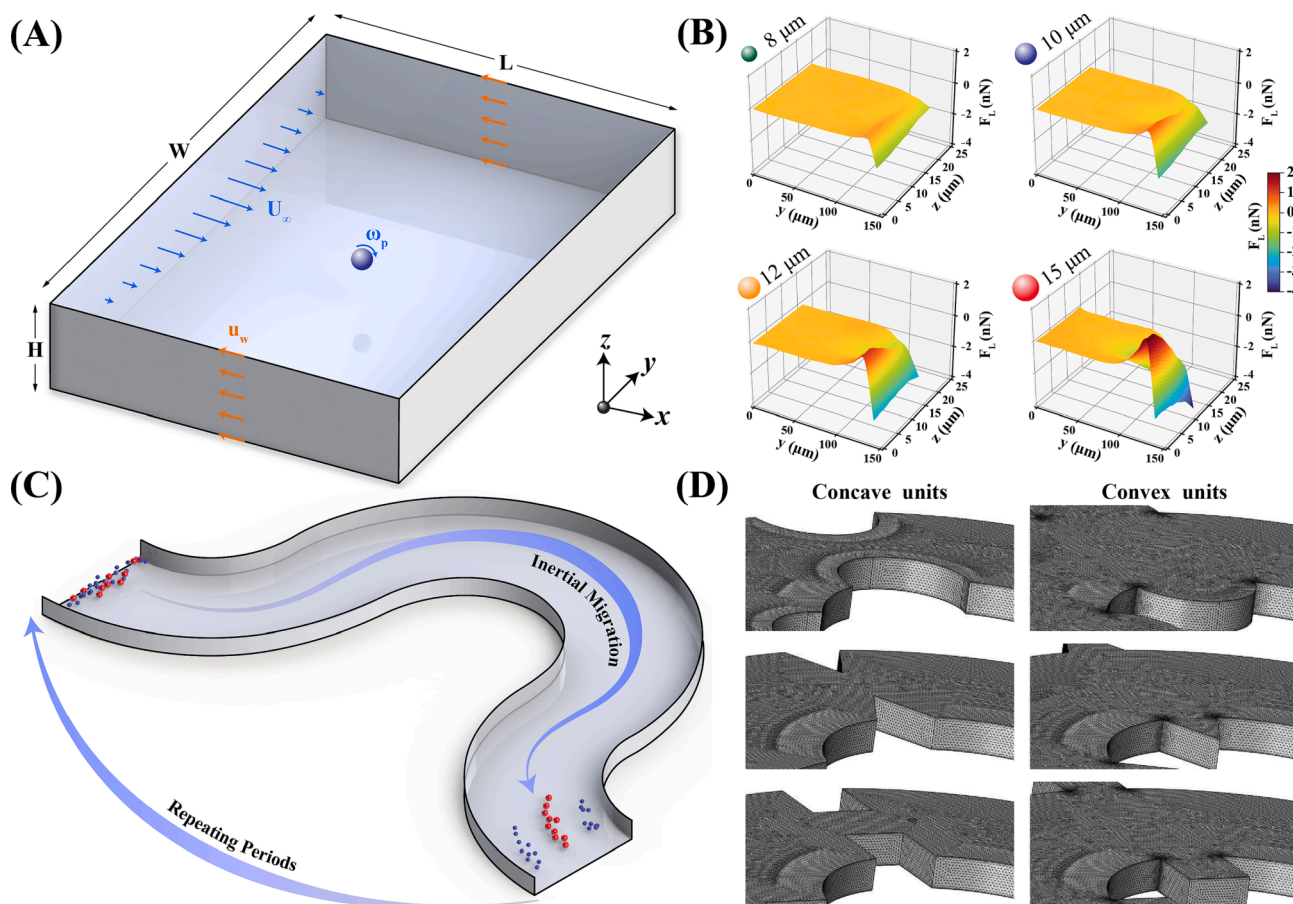
Fig. 2. Numerical modelling of inertial focusing in sinusoidal channels. (A) DNS numerical model transfers into the reference frame of particles for computational ease. (B) The resultant lateral lift forces along the *y*-axis at 1000 μL/min. Due to symmetry, lift force distributions are shown for a quarter of the channel. (C) Conceptual implementation of periodic particle tracing in the periodic channel. Periodic flow is solved for only one period, and particles undergo inertial migration across consecutive channel periods using a user-defined macro. (D) The numerical grids for concave and convex units.

heat-inactivated fetal bovine serum (FBS) and 1% antibiotics under humified atmosphere (37 °C, and 5% CO_2). Cells were then incubated with 100 ng/ml dihexyloxacarbocyanine iodide (DiOC6) for 4 h under the same conditions as above. The incubated cells were detached with TrypLE™ Express Enzyme for 5 min and checked under an Olympus CK40 microscope for detachment. Four mL DMEM medium was added to the flask. Then the stained cells were centrifugated at 700 *g* for 5 min. The cell pellets were redispersed in 6 mL DMEM medium. The stained cells were visualized using a microscope. After that, to quantify the performance of the device on cancer cell separation, the cancer cells were spiked into the diluted whole blood sample (1/20) at a ratio of 0.01%, where the cancer cell concentration was approximately 2.0×10^4 counts/mL.

2.4. Experimental setup and data analysis

The microfluidic devices were placed on the stage of an inverted microscope (Nikon, Eclipse TS100). A syringe pump (SHENCHEN ISPLab02) infused the particle sample into the devices from 100 to 2000 μL/min with an incremental interval of 100 μL/min. A high-speed camera (Photron, FASTCAM SA3) was mounted on the microscope to record the video of particle trajectories using an exposure time of 2 to 50 μs. Each video consists of about 200 frames. We used the open-source software ImageJ (National Institutes of Health) to process and analyze the captured Videos. The separation experiments were carried out to evaluate the performance of the proposed designs. Three criteria, recovery, purity and enrichment, were defined to assess the separation performance. Purity is the ratio of the number of target particles/cells to

the total number of particles/cells at the same outlet/inlet:

$$Purity = \frac{[N_{target}]_{outlet/inlet}}{[N_{total}]_{outlet/inlet}} \tag{1}$$

Recovery (separation efficiency) is the ratio of the number of target particles/cells at the collection outlet to the total number of target particles/cells at the inlet:

$$Recovery = \frac{[N_{target}]_{outlet}}{[N_{target}]_{inlet}} \cong \frac{[N_{target}]_{outlet}}{\sum [N_{target}]_{outlets}} \tag{2}$$

Meanwhile, enrichment is defined as the ratio of the purity of target particles/cells at the specific outlet (P_{outlet}) divided by the purity of target particles/cells at the inlet (P_{inlet}).

$$Enrichment = \frac{P_{outlet}}{P_{inlet}} = \frac{[N_{target}/N_{total}]_{outlet}}{[N_{target}/N_{total}]_{inlet}} \tag{3}$$

3. Numerical modelling

We first calculated the inertial lift force field using direct numerical simulation (DNS). After that, we developed a macro to compute particle positions within each period iteratively by considering inertial lift force, stokes drag force and virtual mass force.

3.1. DNS

The DNS solves the steady-state Navier-Stokes equation for the

laminar flow, including the particle presence and its movement effect on the incompressible Newtonian fluid (Munson et al., 1994):

$$\nabla \bullet V = 0 \tag{4}$$

$$\rho_f (V \bullet \nabla) V = \nabla \bullet [-p \mathbb{I} + \tau], \tau = \mu (\nabla V + (\nabla V)^T) \tag{5}$$

where ∇, V, ρ_f, p, $\mathbb{I}$, τ, μ, and are the spatial gradient operator, fluid velocity vector field, density (1,000 kg/m^3), pressure, identity tensor, fluid shear stress tensor, and dynamic viscosity (0.001 Pa•s), respectively. Fig. 2(A) shows the schematics of the DNS model and boundary
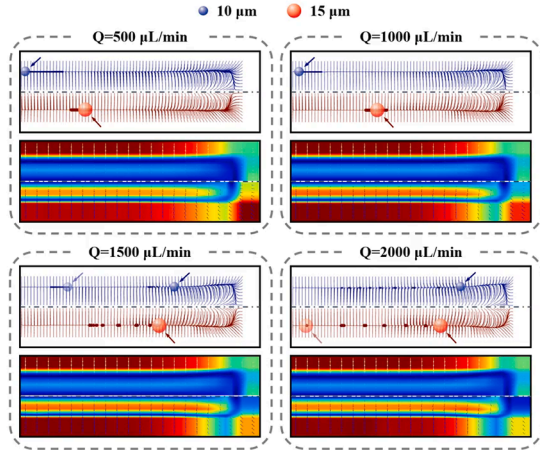
conditions. The channel length was 20 times the particle diameter to ensure the least numerical errors. The inlet and outflow boundaries were adjusted to a constant and fully developed velocity (U_∞) at the matching flow rate. The channel walls were applied with a velocity of particles ($u_w = -u_p$), resulting in a stationary particle state.

Furthermore, the particle's linear and angular velocities (u_p and ω_p) were computed with the assumption that particles are force and torque-free. Di Carlo et al. (Di Carlo et al., 2009) reported this strategy for straight channels, and other researchers later expanded it to curved channels (Dinler and Okumus, 2018; Garcia and Pennathur, 2019). Particle forces (F_p) and moments (M_p) can be calculated by integration of the fluid total stress tensor on the particle's surface:

$$m_p \frac{du_p}{dt} = F_p = -\iint_{S_p} [-p \mathbb{I} + \tau] || dS_p \tag{6}$$

$$I_p \frac{d\omega_p}{dt} = M_p = -\iint_{S_p} (r - r_{cm}) \times [-p \mathbb{I} + \tau] \cdot dS_p \tag{7}$$

where m_p, u_p, t, S_p, I_p, ω_p, r, and r_{cm} indicate the particle mass, particle velocity, auxiliary time, particle surface vector, particle moment of inertia, particle angular velocity vector, location vector, and location of the centre of mass of particles, respectively.

As a result, the cross-sectional lift forces were calculated by adjusting particle velocities while locking particle movement at various channel cross-sectional locations. A recursive gradient descent method was devised in the time domain to calculate the particle velocities, which minimizes the non-lateral fluid force on the particle, resembling a steady-state particle movement. The threshold of the minimization was 0.5% to fulfill the convergence condition. Another crucial point to consider in this scenario is the grid on the particle surface. In terms of computation accuracy and time, the factor of 5% of particle diameter was found to perform best. Different solver settings were evaluated, i.e., using the Lagrange multiplier (Hood et al., 2015); however, all provided

solutions with slight changes. As a result, the Algebraic multigrid (AMG) solver was employed with the Generalized Minimal Residual (GMRES) approach throughout the simulations in the fully coupled scheme.

The numerical modelling was performed for particles ranging from 8 µm to 15 µm. As a result, their cross-sectional lift force distributions were calculated. Fig. 2(B) shows the lateral component of the inertial lift forces at a moderate flow rate of 1,000 µL/min within a quarter of the channel cross-section. Based on the inertial lift force, the cross-sectional migration of 10-µm and 15-µm particles inside a straight channel at various flow rates can be predicted, Video S1.

Supplementary video 1.

3.2. Particle tracing

The Newtonian formulation was used for Lagrangian particle tracing (Sun, 2012):

$$m_p \frac{du_p}{dt} = F_D + F_L + F_{VM} + F_g \tag{8}$$

where the drag force, F_D, is calculated by Stokes' law:

$$F_D = 3\pi a \mu (V - u_p) \tag{9}$$

The lift force F_L was taken from the DNS output. F_{VM}, the virtual mass force that impacts a moving body and its surrounding fluid was taken into account as (Liu et al., 2016):

$$F_{VM} = \frac{1}{2} \left(\frac{1}{6} \pi a^3 \rho_f \right) \frac{d(V - u_p)}{dt} \tag{10}$$

The Stokes number indicates the behaviour of a particle in an accelerating flow (Park and Jung, 2009):

$$St = \frac{\tau_p}{\tau_f} = \frac{\rho_p a^2 / 18\mu}{H / U_M} = \frac{\beta}{18} \kappa Re \tag{11}$$

where τ_p, τ_f, H, U_M, κ, and Re are the particle relaxation, flow characteristic times, channel height, maximum fluid velocity, particle blockage ratio (a/H), and Reynolds numbers ($\rho U_M H / \mu$), respectively. Here, $\beta = \rho_p / \rho_f$ is the specific gravity of particles and is almost valued at 1. Given $St \gg 1$, the particle maintains its initial path rather than flowing down the fluid streamline if the flow direction suddenly changes due to the channel geometry. Finally, in comparison to the order of magnitude of other prominent forces, the gravitational force, F_g, is neglected.

The conceptual implementation of the particle tracing approach is illustrated in Fig. 2(C). Only one period of curved channels was
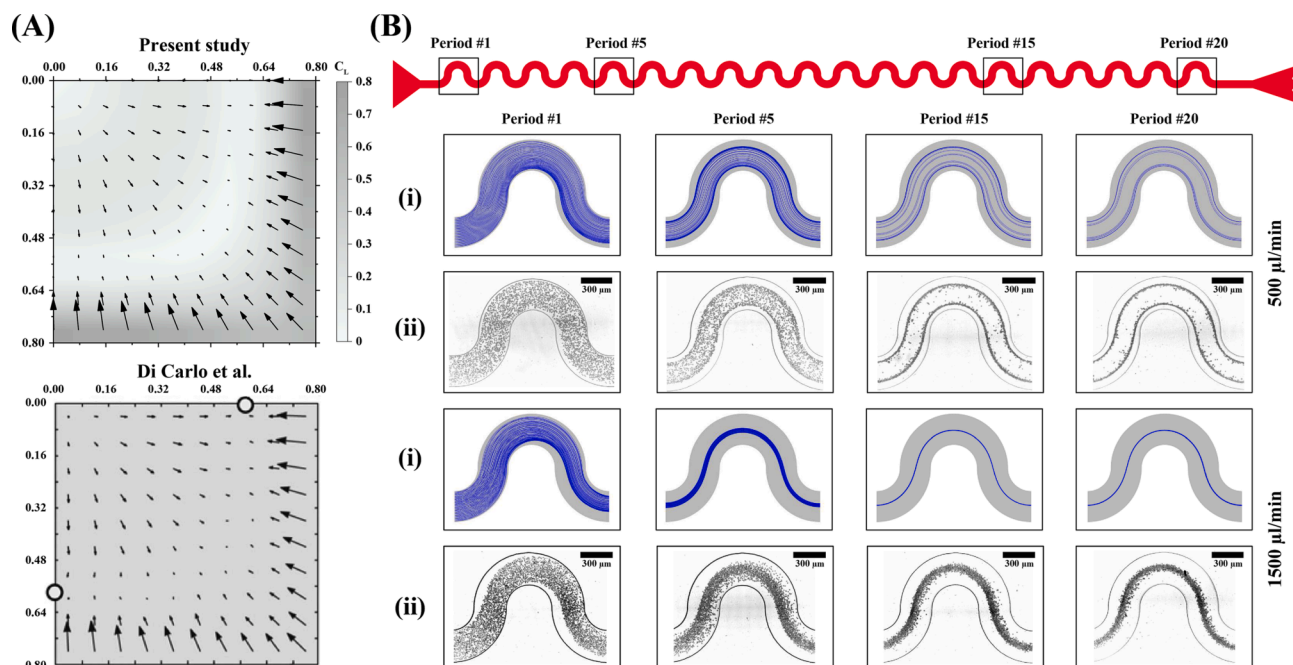
Fig. 3. (A) Numerical modelling validation. (I) The vectors of the inertial lift force in a quarter of the cross section from this work (top) agree with that of Di Carlo's group (bottom) (Di Carlo et al., 2009). The blockage ratio (a/H) = 0.2 and Re = 20. (B) The top-view trajectories of 10-μm particles in the plain sinusoidal channel at flow rates of 500 μL/min and 1500 μL/min, respectively: (i) numerical modelling and (ii) experimental results.

employed to perform the periodic flow calculation. After solving the fluid field, a macro is developed to collect particles at the outlet of one period and place them at the inlet of the next period holding the same relative positions and absolute velocities. The algorithm repeats until it reaches the total period, which is 20 here. This new way of periodic modelling dramatically reduces computational costs and time. Concurrently, it enables an extraordinarily fine grid that best captures the high-velocity gradients and secondary flows and helps converge the solver. The generated grid was consistent through all designs with a maximum element size of 5 μm and less than 6.5 million total elements, as shown in Fig. 2(D). The time step resolution was tuned to a proper order between 10^{-8} to 10^{-6} s by trial and error.

4. Results and discussion

4.1. Validation of the numerical model

We first validated the numerical modelling method of DNS for the inertial lift forces. The vectors of inertial lift force in a quarter of the cross-section of a straight channel were calculated and compared with the reported results from Di Carlo's group (Di Carlo et al., 2009), Fig. 3 (A). We can see a good match between the two plots in both the magnitude of lift forces and particle equilibrium positions. A correct inertial lift force field is essential to predict the focusing pattern of particles because the counterbalance of inertial lift force and Dean drag force determines the final focusing positions of particles in curved channels.

Next, we verified the developed Lagrangian particle tracing model by comparing the simulated particle trajectories with the experimental ones in a plain sinusoidal channel. We simulated the trajectories of 10-μm particles in a plain sinusoidal channel at flow rates of 500 μL/min and 1,500 μL/min, and compared the results with the experimental ones, Fig. 3(B). Depending on the fluid flow rate, the randomly distributed particles migrated laterally towards equilibria near the two sidewalls or the channel centre, depending on the flow rates. The numerical simulation can successfully replicate the particle inertial

focusing process at different periods and the final equilibrium positions observed by experiments (Zhang, 2019). The results prove that the numerical modelling developed in this work is feasible to predict the particle inertial focusing process and can be complementary to experiments.

4.2. Effect of concave and convex obstacle

We designed and fabricated sinusoidal channels with symmetrical micro-obstacles of circular, triangular, and square shapes, respectively, and investigated the effects of obstacle shapes on the inertial focusing of particles. The suspensions of 10-μm and 15-μm particles were infused into these channels with increasing flow rates from 100 μL/min to 1,000 μL/min for the concave channels, and to 2,000 μL/min for the convex channels. Fig. 4 shows the normalized lateral distribution of particles. We can see that the convex formats of the three obstacle shapes (triangle, circular and rectangular) have negligible effects on inertial focusing. In contrast, all three concave obstacles can tune inertial focusing by advancing the transformation of inertial focusing positions from two sidewalls to the channel centre at a lower flow rate, Fig. 4. For example, the flow rates for the transition of the two-sided focusing to the central focusing for 10-μm and 15-μm particles were brought forward from ~ 1,200 μL/min to ~ 400 μL/min and from ~ 1000 μL/min to ~ 300 μL/min, respectively. The concave structures in the channel induce a locally enlarged secondary flow that competes with inertial lift forces and modifies particle focusing positions at a lower flow rate. This is evidenced by the cross-sectional secondary flow field, as shown in Fig. 5. The effect of concave obstacle shape on the advancement of inertial focusing transition is relatively minor, but the size of the concave obstacles significantly affects the transitional flow rates, as illustrated in Fig. 6. For example, even small concave squared obstacles with a size of 50 μm cause particle focusing to occur at a lower flow rate compared to a plain channel. As the size of the concave obstacle increases, the required Reynolds number to convert the two-sided focusing pattern into a single-focusing pattern decreases. These observations provide a basis for designing devices with specific purposes by using concave obstacles of
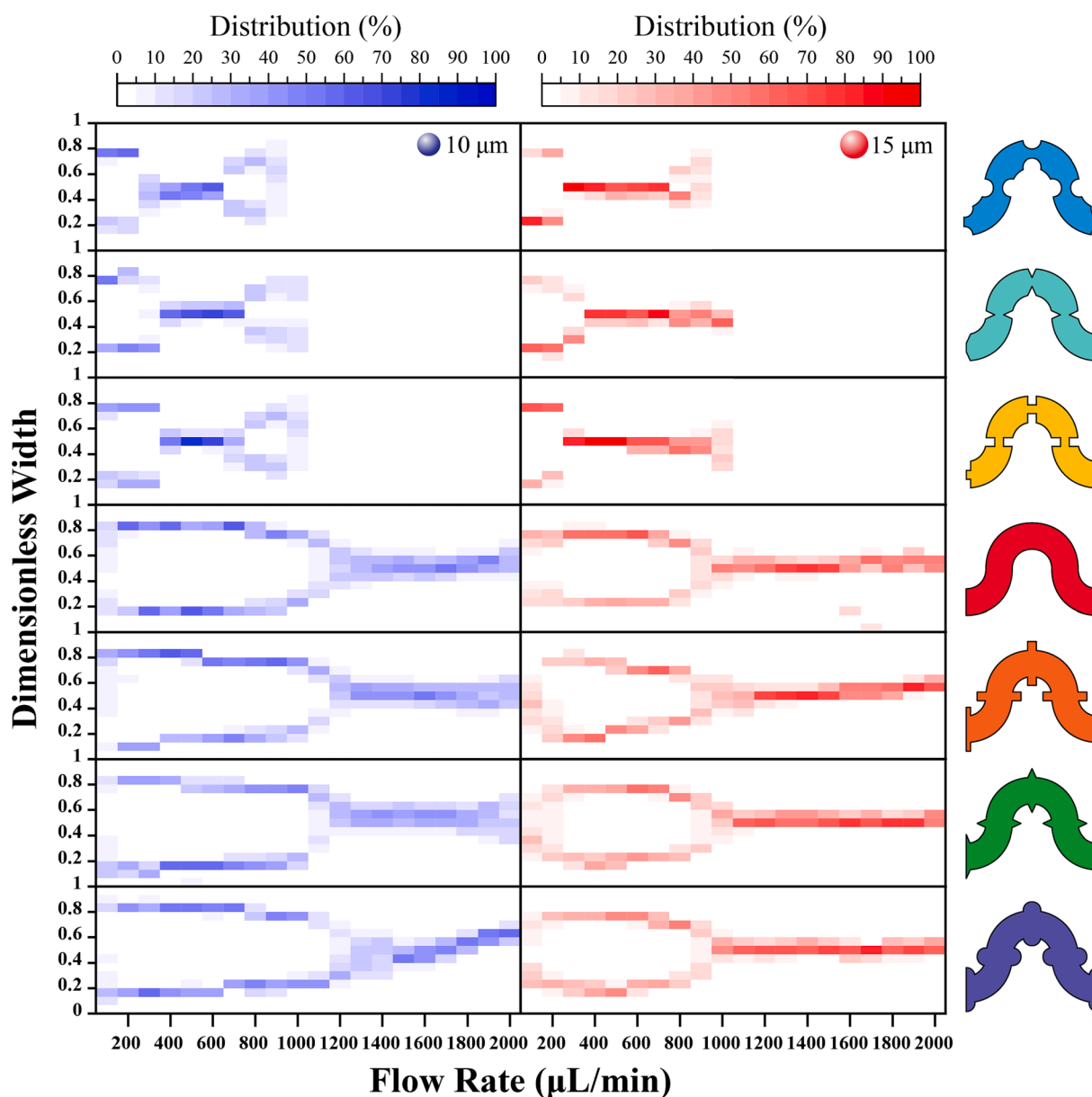
Fig. 4. Experimental distributions of 10- and 15-μm particles along the channel width at the channel outlet. The flow rate is from 100 μL/min to 1000 μL/min for the concave obstacle channels and to 2000 μL/min for the convex obstacle channels.

various sizes. Overall, the local enhancement of Dean flow in concave obstacles is more effective than convex obstacles for adjusting particle focusing.

4.3. Effect of particle size

In this section, we employed numerical simulation to explore the influence of particle size in concave and convex obstacle channels with various shapes, since it could offer various particle sizes with a much wider range. The particle diameters of 8, 10, 12, and 15 μm were released uniformly at the inlet, and their trajectories and final positions were calculated. The distribution of particles at the outlet was depicted as the normalised frequency along the channel width, Fig. 7(A). First, the numerical results generally agree with experimental ones, as evidenced by the particle focusing patterns of 10- and 15-μm particles, Figs. 4 and 7(A). For all the concave and convex obstacle channels, particles focused near two sidewalls at a low flow rate, gradually migrated toward the channel centre when increasing the flow rate, and

finally combined as a single focusing streak above a threshold. The transitional flow rates (Reynolds number) where particles transit from two sidewalls to the channel centre are basically consistent between numerical and experimental results for concave channels, Fig. 7(B).

Second, the larger the particle size was, the lower the transitional flow rate required for the inertial focusing of particles at the channel centre for all the concave and convex obstacle channels with different obstacle shapes, Fig. 7(A) and (B). In addition, the flow rate region of the central focusing mode became wider for larger particles, whereas the flow region of the two-sided focusing mode expanded with the decrease in particle size. Subsequently, the overlap of both flow rate regions enables particle separation based on differential focusing positions at channel centre and near sidewalls.

Finally, the transitional flow rates and Reynolds number for 10- and 12-μm particles overlay because of the insufficient flow rate resolution in the simulation, where the incremental flow rate step was 100 μL/min. Therefore, we used a smaller flow rate step of 20 μL/min and investigated the transitional region in concave channels, Fig. 7(C). In general,
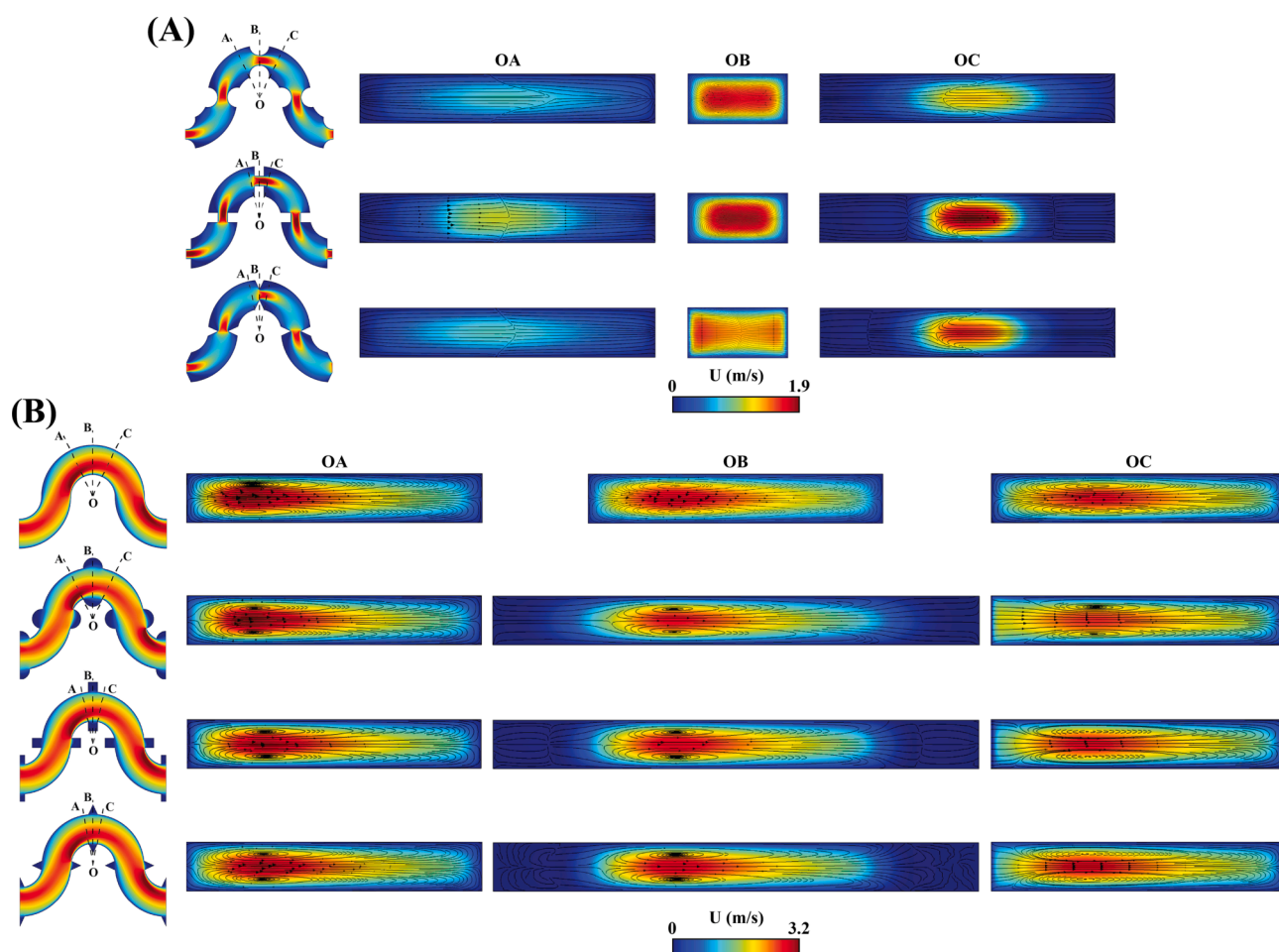
Fig. 5. Cross-sectional secondary velocity fields within (A) the concave-obstacle channels at $Q = 300 \ \mu L/min$ and (B) the plain and convex-obstacle channels at $Q = 1300 \ \mu L/min$. The reason for selecting these specific cross-sections is to capture the key characteristics of each obstacle. With careful consideration, the planes were positioned at the corners of the features in order to study the most significant fluctuations in velocity before, during, and after passing through the obstacles.

we found that the square concave obstacle channels showed a better separation resolution which could separate particles with a minor size difference. For instance, at the flow rate of 350 μL/min, the 8-μm particle can be separated from the 10-μm particles and particles above. At this flow rate, the 8-μm particle is focused along two sidewalls, and 10-μm particles have already focused well at the channel centre. Similarly, at ~ 290 μL/min, 12- and 15-μm particles can be separated based on the differential focusing positions. Furthermore, we used the PMMA particle suspension with a continuous size distribution of 5–20 μm to test the

particle separation cut-off size. The particle suspension was infused into the square concave obstacle channels at 290 μL/min, Fig. 7(D and E) and Video S2. The size distribution at the side and middle outlets indicates that particles below 12 μm and above 14 μm could be decently separated, with a minimum size difference of 2 μm. These results agree with the discovery of Lu et al. (Lu et al., 2020), where the periodic square micro-contractions could improve the separation resolution.
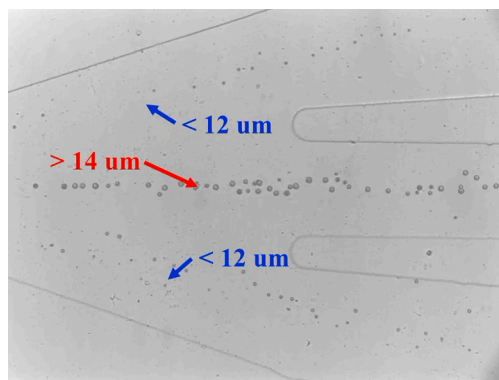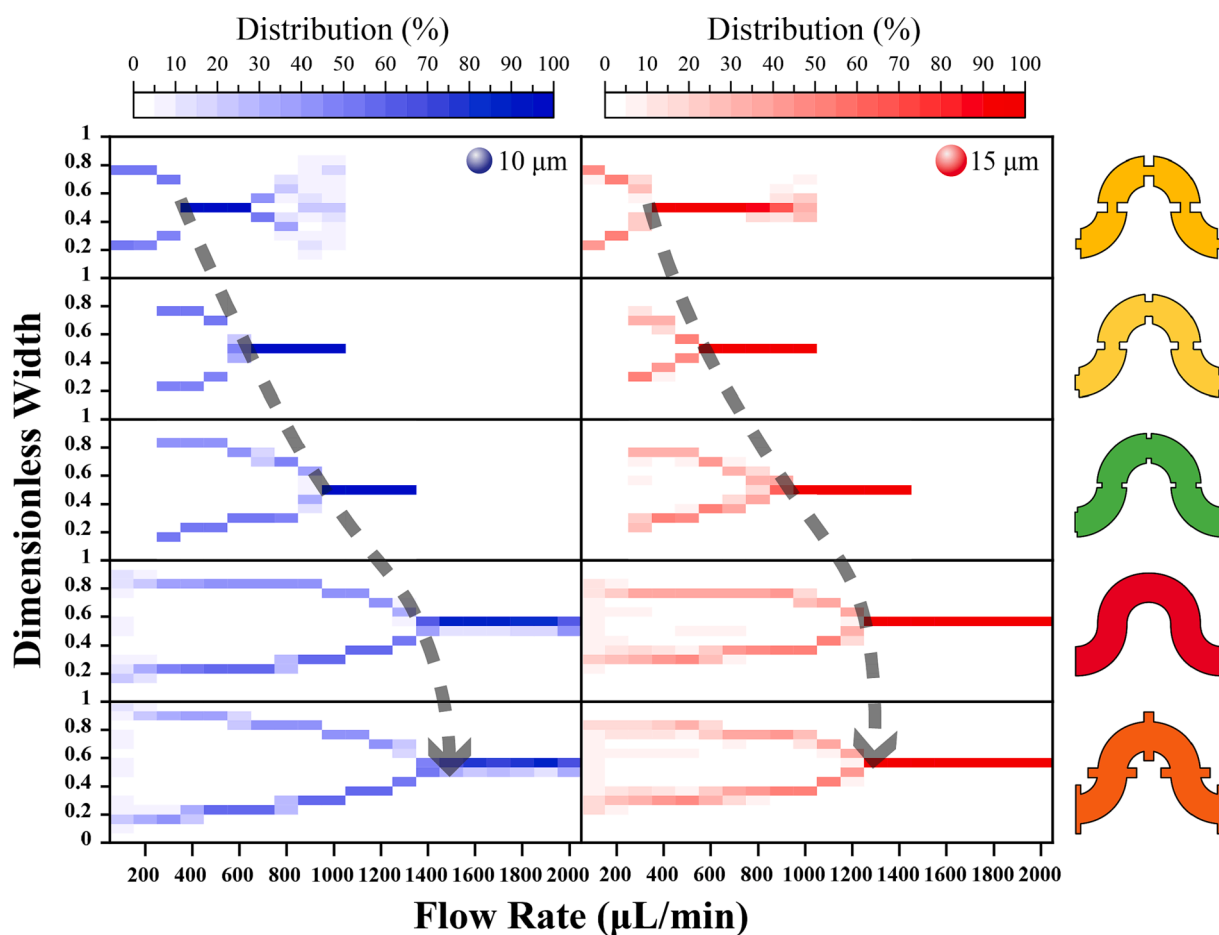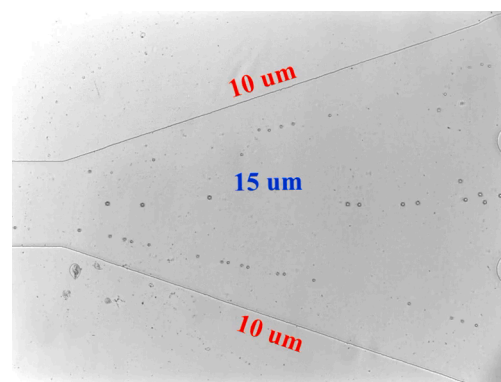

Supplementary video 2.

Fig. 6. Effect of square obstacle size on the transitional flow rates of 10- and 15-μm particles. From top to bottom, square obstacle sizes are −100, −75, −50 (concave), 0 (plain), and + 100 (convex) μm.

4.4. Characterization of separation performance on binary particle mixture

The numerical modelling and experimental tests were conducted to separate binary particle mixture in the square concave obstacle channel to evaluate the separation performance. Fig. 8(A) shows the trajectories of 10- and 15-μm particles at the outlet expansion region under different flow rates by numerical simulation and experiments. At 250 μL/min, both particles were focused along channel sidewalls as double-focusing lines, and the lateral space was insufficient for separation and respective collection. As expected, increasing the flow rate shifted the focusing of 15-μm particles into a single central streak at 290 μL/min and above. In this case, the lateral space of binary particles was enough for a complete separation. The numerical simulation captured the overall trend of inertial separation with excellent accuracy. Furthermore, we experimentally processed the mixture of 10- and 15-μm particles through the optimal square concave obstacle channel at 290 μL/min and collected the separated samples from the central (#1) and sided (#2) outlets, Video S3. The separation performance (i.e., recovery and purity) were excellent just after a single round, above 97% and 96% for both particles, Fig. 8(B-D).

Supplementary video 3.

Besides the particle trajectories from the top-down view, such as the differential focusing process of 10-μm and 15-μm particles at different periods inside the concave square channel, Figure S1, numerical modelling can also provide additional information on particle distribution within various channel cross sections, Fig. 8(E) and supplementary Videos S4 and S5. The numerical simulation showed that uniformly distributed particles quickly migrated vertically toward the top and bottom equilibrium positions and then laterally moved to the sided and central equilibrium positions. In addition, the final equilibrium positions are symmetrical between the top and bottom of the channel cross section. Therefore, the central focusing and two-sided focusing modes have two and four equilibria, respectively.
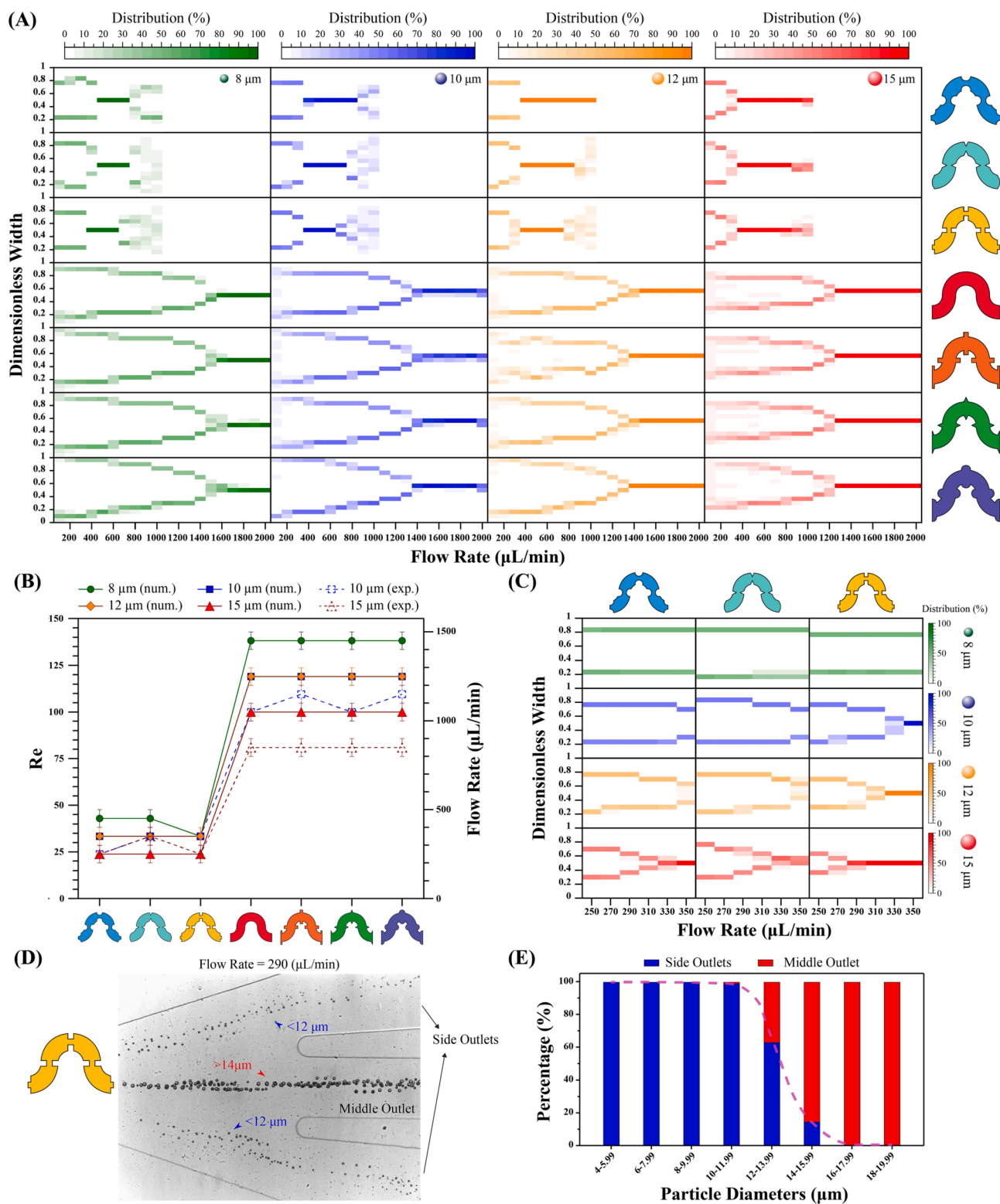
Fig. 7. (A) Numerical prediction of the normalized widthwise distribution of 8-, 10-, 12-, and 15-μm particles in the plain, convex and concave obstacle channel with different obstacle shapes. The particle positions were acquired after the last period. (B) Transitional flow rate and Reynolds numbers for concave and convex obstacle channels with different obstacle shapes. (C) The magnified window of inertial focusing in the three concave channels at the flow rates of 250 to 350 μL/min. The flow rate step is 20 μL/min. The squared concave channel shows the capacity to separate particles with a smaller size difference. (D) Snapshot of particle separation at the outlet in concave square obstacle channel at 290 μL/min. (E) The normalized distribution of variously sized particles at the side and middle outlets. Particle diameter ranges from 4 to 20 μm. It indicates that particles below 12 μm and above 14 μm can be effectively separated.
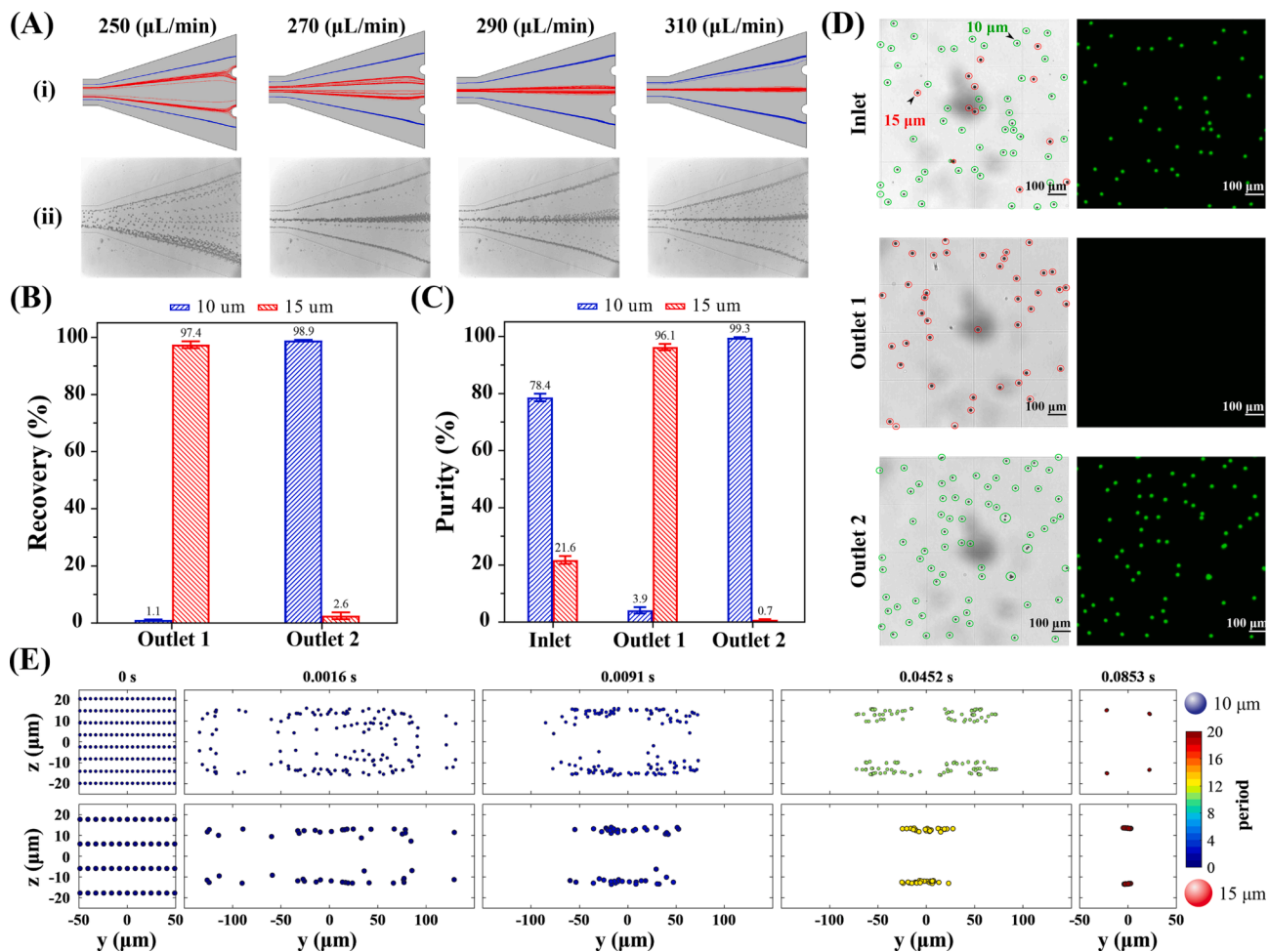
Fig. 8. (A) Trajectories of 10- and 15-μm particles at the outlet expansion region under different flow rates by (i) numerical simulation and (ii) experiments. (B) Recovery and (C) purity of 10- and 15-μm particles at 290 μL/min. (D) Microscopic images of samples collected from the inlet and two outlets. (E) The cross-sectional distribution of particles at different channel locations. The position of cross sections within the sinusoidal channel is colour-coded on particles. The uniformly-distributed particles migrated vertically toward the top and bottom equilibrium positions and then transversely moved to the sided and central equilibrium positions. The square shape of the initial and final stages in the cross-sectional views stems from the local shrinkage of the geometry.
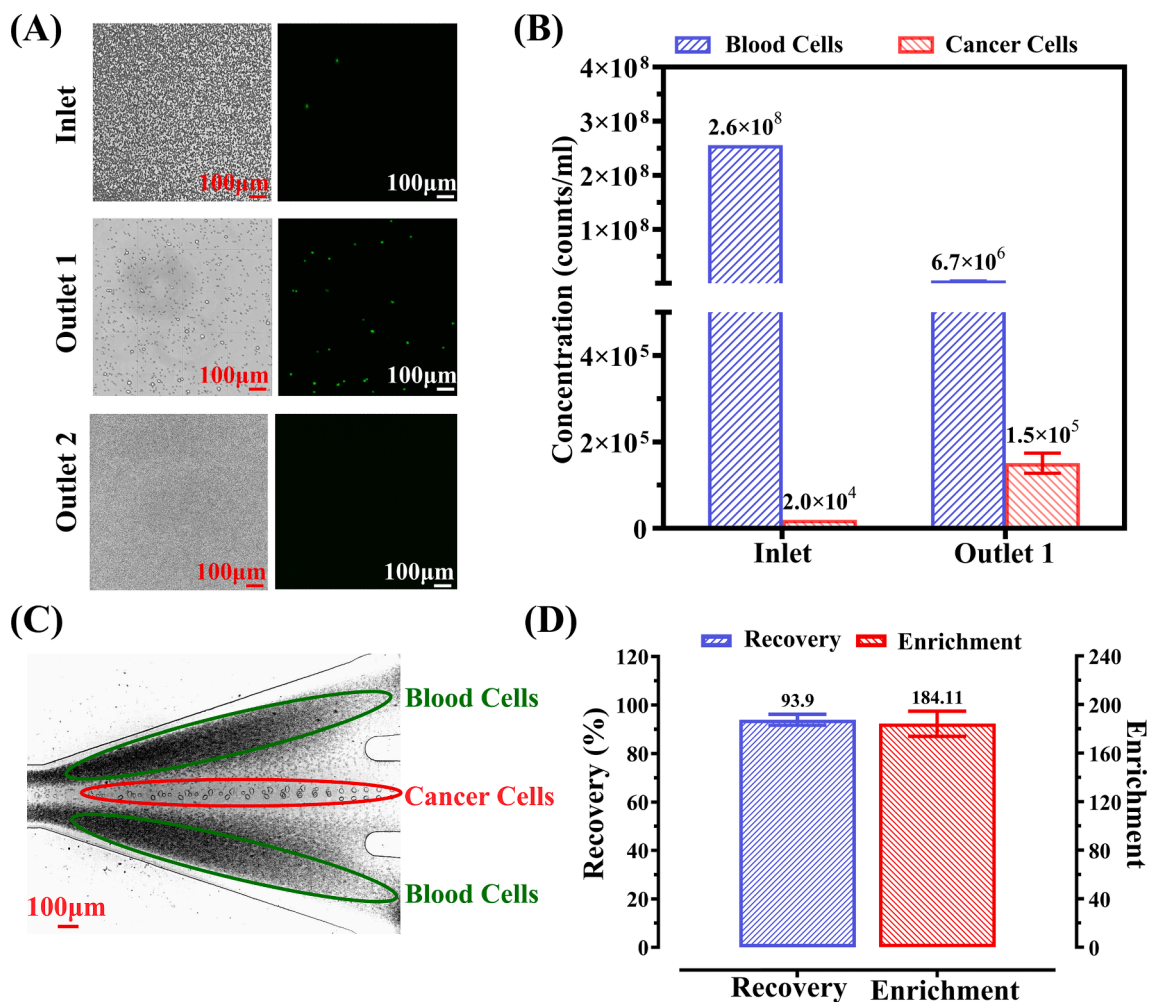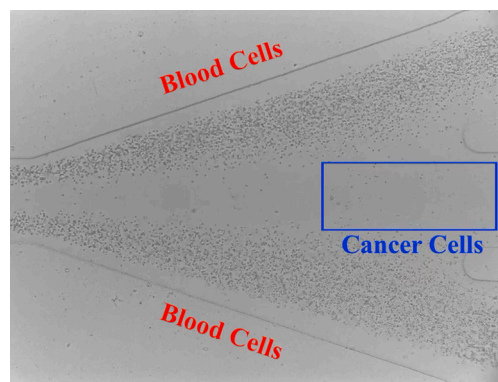

Supplementary video 4.

Supplementary video 5.
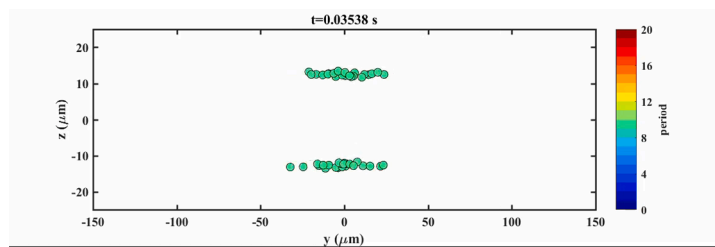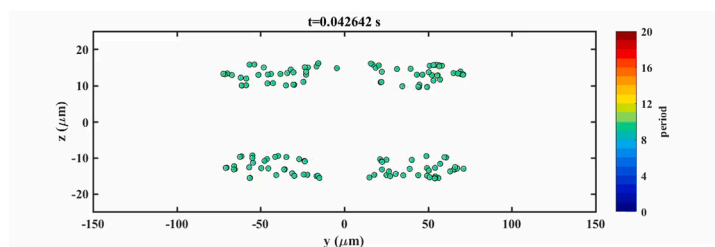
Fig. 9. (A) Microscopic images of blood samples at the inlet and two outlets under a haemocytometer. Only the cancer cells are stained with green fluorescence. (B) The concentration of the blood and cancer cells before and after single processing through the device. (C) High-speed image shows the distribution of blood and cancer cells at the trifurcation area of the channel. (D) The recovery (or separation efficiency) and enrichment of cancer cells after one single processing. (For interpretation of the references to colour in this figure legend, the reader is referred to the web version of this article.)

4.5. Separation of cancer cells from blood cells

Based on the above fundamental study, we developed a high-resolution microfluidic cell separation device based on the optimal square concave obstacle channel. Then, we applied the developed device to separate cancer cells from the whole blood to demonstrate its application in biological cells. We spiked the fluorescently labelled Human Glioblastoma cells (U87MG) in a diluted (20 ×) whole blood sample at a ratio of 0.011%. The size of the cancer cells was from 14 to 20 μm, with the most in the region of 16–18 μm, larger than most of the blood cells (platelets, red blood cells, white blood cells, approximately 1–3, 6–8, 10–15 μm, respectively). We infused the mixture samples into the square concave obstacle channel at 290 μL/min. We collected the samples from both outlets and analyzed the separation performance, Video S6. Fig. 9 (A) shows the brightfield and fluorescence images of blood samples from the inlet and the two outlets. At the inlet, there were massive background blood cells, and it was challenging to detect the cancer cells. After single processing through the proposed microfluidic device, cancer cells were highly enriched, and background blood cells were significantly removed at outlet 1, Fig. 9(A). The quantitative data indicated that the concentration of cancer cells was enhanced from 2.0×10^4 counts/mL to 1.5×10^5 counts/mL, while the blood cells were depleted by two orders from 2.6×10^8 counts/mL to 6.7×10^6 counts/

mL, Fig. 9(B). The separation efficiency (or recovery) for cancer cells was as high as 93.9% and most cancer cells can enter the central outlet, Fig. 9(C) and (D). This is attributed to high separation resolution by the square concave obstacle channel.). The high-efficiency separation also significantly enhanced the ratio of cancer cells from 0.01% to 1.94%, with a 184-fold enrichment, Fig. 9(D).

Supplementary video 6.

5. Conclusions

This work numerically and experimentally studied the effects of periodic obstacles on inertial focusing and separation in sinusoidal microchannels. The circular, triangular and square periodic micro-obstacles were embedded into the channels to form the convex and concave obstacles. We developed numerical modelling method to successfully predict the focusing trajectories of particles in various concave and convex obstacle channels. The convex obstacles have negligible modification on inertial focusing, but concave obstacles can advance the flow rate for the transition of inertial focusing positions. In addition, the square concave obstacles could enhance particle separation resolution up to 2 μm. Finally, we developed a high-resolution microfluidic device based on the square concave obstacle for the separation of various-sized particles and cancer cells from the blood. This study provides new insight into choosing a suitable obstacle shape in curvilinear channels to optimize particle separation.

Declaration of Competing Interest

The authors declare that they have no known competing financial interests or personal relationships that could have appeared to influence the work reported in this paper.

Data availability

Data will be made available on request.

Acknowledgements

Appendix A. Supplementary material

Supplementary data to this article can be found online at https://doi.org/10.1016/j.ces.2023.118826.

References

Amini, H., Lee, W., Di Carlo, D., 2014. Inertial microfluidic physics. Lab Chip 14 (15), 2739–2761.

Asghari, M., Serhatlioglu, M., Saritas, R., Guler, M.T., Elbuken, C., 2019. Tape'n roll inertial microfluidics. Sens. Actuators, A 299, 111630.

B. Munson, D. Young, and T. Okiishi, "Fundamentals of fluid mechanics, Fundam. Fluid Mech.(1994)," ed.

Bazaz, S.R., Mashhadian, A., Ehsani, A., Saha, S.C., Krüger, T., Warkiani, M.E., 2020. Computational inertial microfluidics: a review. Lab Chip 20 (6), 1023–1048.

Bhagat, A.A.S., Kuntaegowdanahalli, S.S., Papautsky, I., 2008. Enhanced particle filtration in straight microchannels using shear-modulated inertial migration. Phys. Fluids 20, 101702.

Cha, H., et al., 2022. Tuning particle inertial separation in sinusoidal channels by embedding periodic obstacle microstructures. Lab Chip 22 (15), 2789–2800.

Chen, Z., et al., 2019. River meander-inspired cross-section in 3D-printed helical microchannels for inertial focusing and enrichment. Sens. Actuators B 301, 127125.

S. Choi and J. K. Park, "Hydrophoresis: A New-Phoretic Method for High-Resolution Particle Separation," in *Actuators and Microsystems Conference*, Lyon 2007: IEEE, pp. 1769-1772.

Collins, D.J., Alan, T., Neild, A., 2014. Particle separation using virtual deterministic lateral displacement (vDLD). Lab Chip 14 (9), 1595–1603.

Dalili, A., Montazerian, H., Sakthivel, K., Tasnim, N., Hoorfar, M., 2021. Dielectrophoretic manipulation of particles on a microfluidics platform with planar tilted electrodes. Sens. Actuators B 329, 129204.

D'Avino, G., Greco, F., Maffettone, P.L., 2017. Particle migration due to viscoelasticity of the suspending liquid and its relevance in microfluidic devices. Annu. Rev. Fluid Mech. 49, 341–360.

Di Carlo, D., Edd, J.F., Humphry, K.J., Stone, H.A., Toner, M., 2009. Particle segregation and dynamics in confined flows. Phys. Rev. Lett. 102 (9), 94503.

Di Carlo, D., 2009. Inertial microfluidics. Lab Chip 9 (21), 3038–3046.

Dinler, A., Okumus, I., 2018. Inertial particle separation in curved networks: a numerical study. Chem. Eng. Sci. 182, 119–131.

Garcia, M., Pennathur, S., 2019. A model for inertial particles in curvilinear flows. Microfluid. Nanofluid. 23 (5), 1–9.

Hochstetter, A., et al., 2020. Deterministic lateral displacement: Challenges and perspectives. ACS Nano 14 (9), 10784–10795.

Hood, K., Lee, S., Roper, M., 2015. Inertial migration of a rigid sphere in three-dimensional Poiseuille flow. J. Fluid Mech. 765, 452–479.

Huang, L.R., Cox, E.C., Austin, R.H., Sturm, J.C., 2004. Continuous particle separation through deterministic lateral displacement. Science 304 (5673), 987–990.

Kim, J.A., Lee, J., Wu, C., Nam, S., Di Carlo, D., Lee, W., 2016. Inertial focusing in non-rectangular cross-section microchannels and manipulation of accessible focusing positions. Lab Chip 16 (6), 992–1001.

Kuntaegowdanahalli, S.S., Bhagat, A.A.S., Kumar, G., Papautsky, I., 2009. Inertial microfluidics for continuous particle separation in spiral microchannels. Lab Chip 9 (20), 2973–2980.

Lee, M.G., Shin, J.H., Bae, C.Y., Choi, S., Park, J.-K., 2013. Label-free cancer cell separation from human whole blood using inertial microfluidics at low shear stress. Anal. Chem. 85 (13), 6213–6218.

Li, M., et al., 2016. Inertial focusing of ellipsoidal Euglena gracilis cells in a stepped microchannel. Lab Chip 16 (22), 4458–4465.

Lin, S.-C.-S., Mao, X., Huang, T.J., 2012. Surface acoustic wave (SAW) acoustophoresis: now and beyond. Lab Chip 12 (16), 2766–2770.

Liu, C., Xue, C., Sun, J., Hu, G., 2016. A generalized formula for inertial lift on a sphere in microchannels. Lab Chip 16 (5), 884–892.

Lu, X., Liu, C., Hu, G., Xuan, X., 2017. Particle manipulations in non-Newtonian microfluidics: a review. J. Colloid Interface Sci. 500, 182–201.

Lu, X., Chow, J.J.M., Koo, S.H., Tan, T.Y., Jiang, B., Ai, Y., 2020. Enhanced molecular diagnosis of bloodstream candida infection with size-based inertial sorting at submicron resolution. Anal. Chem. 92 (23), 15579–15586.

Martel, J.M., Toner, M., 2013. Particle focusing in curved microfluidic channels. Sci. Rep. 3, 3340.

Martel, J.M., Toner, M., 2014. Inertial Focusing in Microfluidics. Annu. Rev. Biomed. Eng. 16, 371–396.

Nam-Trung, N., 2012. Micro-magnetofluidics: interactions between magnetism and fluid flow on the microscale. Microfluid Nanofluid 12, 1–16.

Nathamgari, S.S.P., et al., 2015. Isolating single cells in a neurosphere assay using inertial microfluidics. Lab Chip 15 (24), 4591–4597.

Paiè, P., Bragheri, F., Di Carlo, D., Osellame, R., 2017. Particle focusing by 3D inertial microfluidics. Microsyst. Nanoeng. 3 (1), 1–8.

Pamme, N., 2006. Magnetism and microfluidics. Lab Chip 6 (1), 24–38.

Pappas, D., Wang, K., 2007. Cellular separations: a review of new challenges in analytical chemistry. Anal. Chim. Acta 601 (1), 26–35.

Park, J.-S., Jung, H.-I., 2009. Multiorifice flow fractionation: Continuous size-based separation of microspheres using a series of contraction/expansion microchannels. Anal. Chem. 81 (20), 8280–8288.

Pethig, R., 2010. Dielectrophoresis: Status of the theory, technology, and applications. Biomicrofluid 4 (2), 022811.

Ren, H., et al., 2021. Multiplexed serpentine microchannels for high-throughput sorting of disseminated tumor cells from malignant pleural effusion. Sens. Actuators B, 129758.

Rodriguez-Mateos, P., Ngamsom, B., Dyer, C.E., Iles, A., Pamme, N., 2021. Inertial focusing of microparticles, bacteria, and blood in serpentine glass channels. Electrophoresis 42 (21–22), 2246–2255.

Segre, G., 1961. Radial particle displacements in Poiseuille flow of suspensions. Nature 189, 209–210.

Shen, S., et al., 2017. Spiral microchannel with ordered micro-obstacles for continuous and highly-efficient particle separation. Lab Chip 17 (21), 3578–3591.

Shi, X., Tan, W., Lu, Y., Cao, W., Zhu, G., 2021. A needle tip CCEA microfluidic device based on enhanced Dean flow for cell washing. Microsyst. Nanoeng. 7 (1), 81.

Sun, J., et al., 2012. Double spiral microchannel for label-free tumor cell separation and enrichment. Lab Chip 12 (20), 3952–3960.

Tang, W., Zhu, S., Jiang, D., Zhu, L., Yang, J., Xiang, N., 2020. Channel innovations for inertial microfluidics. Lab Chip 20 (19), 3485–3502.

Tay, H.M., et al., 2021. Direct isolation of circulating extracellular vesicles from blood for vascular risk profiling in type 2 diabetes mellitus. Lab Chip 21 (13), 2511–2523.

Thompson, A., Paguirigan, A., Kreutz, J., Radich, J., Chiu, D., 2014. Microfluidics for single-cell genetic analysis. Lab Chip 14 (17), 3135–3142.

Warkiani, M.E., Tay, A.K.P., Khoo, B.L., Xiaofeng, X., Han, J., Lim, C.T., 2015. Malaria detection using inertial microfluidics. Lab Chip 15, 1101–1109.

Whitesides, G.M., 2006. The origins and the future of microfluidics. Nature 442 (7101), 368–373.

Whitesides, G.M., Ostuni, E., Takayama, S., Jiang, X., Ingber, D.E., 2001. Soft lithography in biology and biochemistry. Annu. Rev. Biomed. Eng. 3 (1), 335–373.

Wu, L., Guan, G., Hou, H.W., Bhagat, A.A.S., Han, J., 2012. Separation of leukocytes from blood using spiral channel with trapezoid cross-section. Anal. Chem. 84 (21), 9324–9331.

Yan, S., et al., 2018. A portable, hand-powered microfluidic device for sorting of biological particles. Microfluid. Nanofluid. 22 (1), 8.

Ying, Y., Lin, Y., 2019. Inertial focusing and separation of particles in similar curved channels. Sci. Rep. 9 (1), 16575.

Zhang, J., et al., 2016. Fundamentals and applications of inertial microfluidics: a review. Lab Chip 16 (1), 10–34.

Zhang, J., et al., 2019. Fundamentals of differential particle inertial focusing in symmetric sinusoidal microchannels. Anal. Chem. 91 (6), 4077–4084.

Zhang, J., Yan, S., Sluyter, R., Li, W., Alici, G., Nguyen, N.-T., 2014. Inertial particle separation by differential equilibrium positions in a symmetrical serpentine microchannel. Sci. Rep. 4, 4527.

Zhao, L., Gao, M., Niu, Y., Wang, J., Shen, S., 2022. Flow-rate and particle-size insensitive inertial focusing in dimension-confined ultra-low aspect ratio spiral microchannel. Sens. Actuators B 369, 132284.

Zhou, J., Giridhar, P.V., Kasper, S., Papautsky, I., 2013. Modulation of aspect ratio for complete separation in an inertial microfluidic channel. Lab Chip 13 (10), 1919–1929.

Zhou, J., Papautsky, I., 2013. Fundamentals of inertial focusing in microchannels. Lab Chip 13 (6), 1121–1132.

Zhou, J., Papautsky, I., 2021. Resolving dynamics of inertial migration in straight and curved microchannels by direct cross-sectional imaging. Biomicrofluid 15 (1), 014101.

Electronic Supporting Information

Effects of obstacles on inertial focusing and separation in sinusoidal channels: an experimental and numerical study

Haotian Cha[+a], Hoseyn A. Amiri[+b,c], Sima Moshafi[+d,e], Ali Karimi[f], Ali Nikkhah[g], Xiangxun Chen[a], Hang T. Ta[a,h], Nam-Trung Nguyen*[a], Jun Zhang*[a]

[a] Queensland Micro- and Nanotechnology Centre, Griffith University, Nathan, Queensland 4111, Australia.
[b] Department of Biomechanics, School of Mechanical Engineering, Iran University of Science and Technology, Narmak, Tehran, 16846-13114, Iran.
[c] George W. Woodruff School of Mechanical Engineering, Parker H. Petit Institute for Bioengineering and Biosciences, Georgia Institute of Technology, Atlanta, GA 30332, USA
[d] Department of Mechanical Engineering, Faculty of Engineering, Kharazmi University, Tehran, 15719-14911, Iran.
[e] Department of Mathematics and Statistics, Georgia State University, Atlanta, GA 30303, USA
[f] Department of Chemical and Petroleum Engineering, Sharif University of Technology, Tehran, 14588-89694, Iran.
[g] Department of Mechanical and Aerospace Engineering, University at Buffalo, The State University of New York, Buffalo, NY 14260, USA.
[h] Bioscience Discipline, School of Environment and Science, Griffith University, Nathan, Queensland 4111, Australia
[+] Equally contributed.

* Correspondence E-mails: nam-trung.nguyen@griffith.edu.au; jun.zhang@griffith.edu.au

Table of Contents

Video S6. Inertial separation of Glioblastoma (U87MG) cancer cells from blood in the square concave obstacle channel. Q=290 μL/min.

Figure S1 Top view of 10-µm (blue) and 15-µm (red) particle trajectory simulation in the square concave channel at Q=290 µL/min.

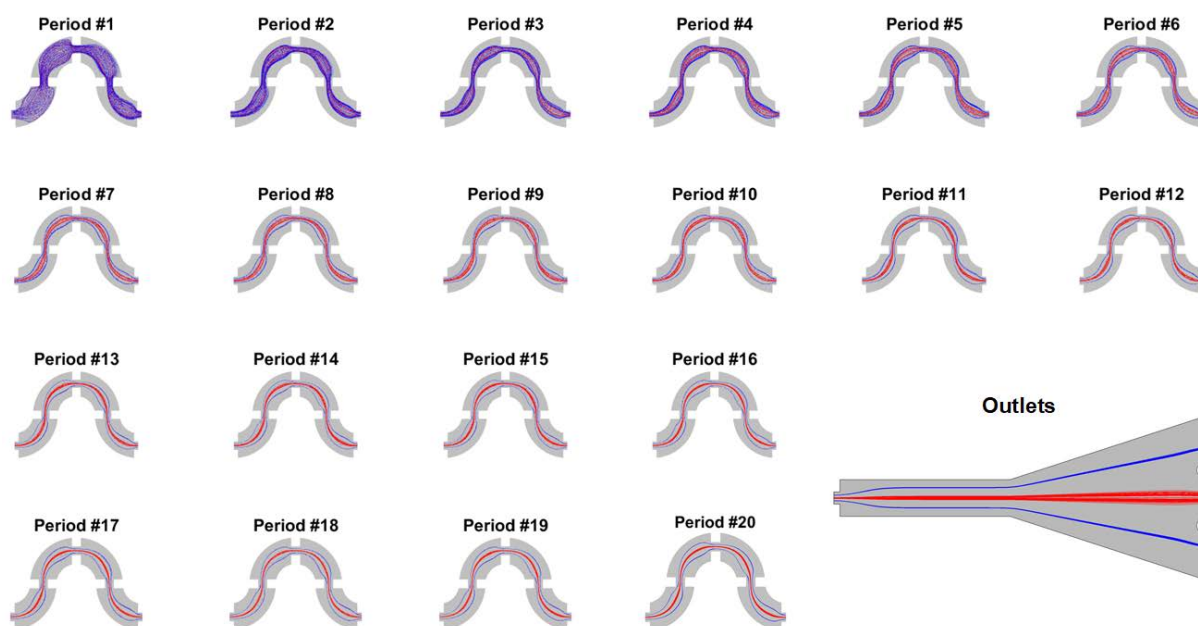**Figure S1** Top view of 10-µm (blue) and 15-µm (red) particle trajectory simulation in the square concave channel at Q=290 µL/min.

Video S1. Lift distribution and cross-sectional migration of 10- and 15-μm particles inside the straight channels at various flow rates.

The DNS model for a relatively long straight channel has been investigated to capture the particle's final equilibria by analyzing the cross-sectional particle trajectories. Video S1 shows that lift forces and particle distributions are directly linked to particle migrations. The transparency of particles placed over the video marks the instability of those positions. This means that even slight uncertainties, likely in the experiments, can shift particles toward their stable positions (less transparent particles). The aspect ratio used here is the same as sinusoidal channels in this work. Due to the symmetry, only a quarter of the cross section is shown for each particle.

Video S2. The distribution of particles with continuous size (5-20 μm) at the outlet in concave square obstacle channel. Q=290 μL/min.

Video S3. Inertial separation of 10-μm and 15-μm polystyrene beads in the square concave obstacle channel. Q=290 μL/min.

Video S4. Cross-sectional migration of 10-μm particles inside the concave square channel at Q=290 μL/min.

Video S5. Cross-sectional migration of 15-μm particles inside the concave square channel at Q=290 μL/min.

Video S6. Inertial separation of Glioblastoma (U87MG) cancer cells from blood in the square concave obstacle channel. Q=290 μL/min.